Please cite this article as: Tianwei Sun, Lingyun Peng*, Xiaodong Ji, Xiaojun Li . Development of a negative stiffness friction damping device with an amplification mechanism. Engineering Structures, 2023, 115286.

Development of a Negative Stiffness Friction Damping Device with an Amplification Mechanism

Tianwei Sun[a,b], Lingyun Peng[a,*], Xiaodong Ji[b], Xiaojun Li[a]

[a] Beijing Key Lab of Earthquake Engineering and Structural Retrofit, Beijing University of Technology, Beijing, China

[b] Department of Civil Engineering, Tsinghua University, Beijing, China

ABSTRACT: This paper proposes an innovative negative stiffness friction damping device (NSFDD), which is characterized with a combination of negative stiffness and friction damping force. The large force capacity of the NSFDD is realized by the amplification mechanism of a two-consecutive lever and using the pre-compressed gas springs. A mechanical model is developed to represent the force-displacement relationship of the proposed NSFDD. The influence of key parameters on the NSFDD performance is analyzed using this mechanical model and demonstrates the advantage of using pre-compressed gas springs. A NSFDD specimen was manufactured and examined by experimental tests. The NSFDD specimen exhibits an obvious negative stiffness and stable energy dissipation, demonstrating the feasibility and effectiveness of the NSFDD. Finally, a refined finite element (FE) model is developed to represent the NSFDD. Both the experimental tests and FE simulation validate the accuracy of the mechanical model of the NSFDD.

Keywords: Negative stiffness; Friction damping; Amplification mechanism; Mechanical model; Experimental test.

1 Introduction

The objective of seismic protection is to reduce the force demand and control the lateral deformation of a structure subjected to strong ground motions. In the last few decades, the vibration control techniques have been developed for control the seismic responses of buildings and infrastructures [1,2]. Extensive achievements have been made in this field, such as base isolation and energy dissipation technologies. Among these technologies, negative stiffness vibration control shows a unique characteristic, which decreases the entire stiffness of the system to reduce acceleration response [3]. Negative stiffness means that a force is introduced to assist motion, not to oppose it [4]. The concept of negative stiffness was first proposed by Molyneaux [5] in 1957. Based on the mechanisms of negative stiffness, existing negative stiffness technologies are categorized into the following types: negative stiffness metamaterials [6], buckled beams [7], pre-compression springs [8], magnets [9], and magnetorheological technology [10], etc.

Thus far, the negative stiffness technology has been extensively developed in mechanical engineering [11,12] and materials science fields [13-16]. Wang et al. [17,18] designed a variety of novel multistable metamaterials which were based on mechanisms in the biological organs. The materials have negative stiffness effects, snap-through behaviors, higher mechanical performance and lower density. The sleeve-type negative stiffness [19,20] is a novel type negative stiffness metamaterial that can dissipate mechanical energy even if the metamaterial is only composed of one negative stiffness cell, having a wide range of application prospects in many engineering fields. Meng [21] presented negative stiffness oscillators that were realized through Euler buckled beams and showed great potential to construct tunable broadband vibration absorption configurations. Robertson [22] used the arrangement of magnets to produce a negative stiffness element to reduce the natural frequency of the system. Mehreganian [23] investigated the negative stiffness honeycomb metamaterials made of double curved beams and the desired negativity in the stiffness matrix could be achieved with high bistability ratios. Anastasio et al. [24-27] tested a negative stiffness oscillator to exploit its linear and nonlinear dynamics and chaotic motion as well. The oscillator exhibits a strong nonlinear behavior, mainly due to its polynomial elastic restoring force with a negative stiffness region. In addition, the results show that negative stiffness has the advantages, such as damping augmentation and reduced acceleration transmissibility.

In the civil engineering field, Iemura et al. [10,28,29] introduced the negative stiffness technique to control structural dynamic responses by reducing structural stiffness and adding damping. They developed a magnetorheological fluid-based negative stiffness damper and negative stiffness friction damper (which works in a similar way to friction pendulum sliding). Das [30] proposed the shape memory alloy (SMA)-based nonlinear energy sink with negative stiffness and friction. A number of parametric studies demonstrate its enhanced and robust performance. The negative stiffness technology can improve the vibration isolation performances [31-33] and the simulation results indicate that vibration isolators with negative stiffness could have smaller displacement amplitude and force transmissibility peaks, and a wider isolation frequency band. Cimellaro [34] proposed a three-dimensional (3-D) base isolation system with a negative stiffness device, which could reduce the vertical acceleration and the input energy transferred to the superstructure. Javanbakht [35-37] proposed an analysis model for the negative stiffness dampers which was employed to analyze the response control of stay cables, demonstrating the effectiveness of the negative stiffness technique for cable control. Walsh et al. [38,39] proposed a variable negative stiffness device used to improve seismic protection by apparent weakening, and investigated the effect of supplemental damping in the structure on the control performance of the systems. Pasala and Sarlis [3,4,40,41] proposed a negative stiffness device with an amplification mechanism that effectively amplifies the negative stiffness. Furthermore, a viscous damper was added along with the negative stiffness device to control the displacement response of the structure induced by stiffness reduction. Nagarajaiah et al. [42-47] investigated the dynamic responses of various types of structural system (multi-story steel frame, bridge, tall building with damped outrigger) incorporated with the negative stiffness devices. Both experimental tests and numerical simulation indicate that the control of displacement and acceleration responses, as well as the possibility of structural damage, can be achieved by a combination of negative stiffness and supplemental damping. Antoniadis [48-50] proposed KDamping which used negative stiffness to indirectly increase the inertia effect of the additional mass. Peng [51] proposed a negative stiffness damping mechanism that could provide negative stiffness and friction damping simultaneously.

While the various types of negative stiffness devices have been developed, the force capacity of the devices is relatively small compared to the large force demand in civil engineering. To this end, this paper proposes a novel passive negative stiffness friction damping device (NSFDD) which includes a two-consecutive lever mechanism to amplify the negative stiffness and friction damping force significantly. The major contribution of this paper is to develop a mechanical model of this device and validate its cyclic performance. Section 2 presents the mechanism of the devices, including the generation of negative stiffness and friction damping force, and the amplification mechanism of the two-consecutive lever. Section 3 develops the mechanical model of the NSFDD. Using this model, the influence of key design parameters of the devices are assessed using parametric analysis. Section 4 describes experimental tests of the NSFDD subjected to cyclic lateral loads to examine its hysteretic behavior, negative stiffness, and energy dissipation capacity. Finally, a finite element model is developed for this device. Both the finite element analyses and experimental results validate the proposed mechanical model of this device.

2 Mechanism of the NSFDD

2.1 Principle of negative stiffness and friction damping

Existing passive negative stiffness devices are primarily compressed springs driven by a specific device to generate negative stiffness [4]. However, the disadvantage of these devices is that additional damping devices need to be connected to provide damping and control the displacement response that would be enlarged due to reduced stiffness. To produce both negative stiffness and damping simultaneously, the key component of the NSFDD is designed, as illustrated in Fig. 1. As shown in Fig. 1(a), the ends A and B of the rotating rod are hinged to the friction plate and the upper part, respectively. The upper part only moves vertically and is always compressed by the vertical force *P*. The force *P* compresses the friction plate through the rotating rod. The friction plate is in contact with the friction surface and can move horizontally. When the friction plate generates displacement x, as depicted in Fig. 1(b), the rotating rod is driven to rotate. The vertical force P generates the force P_α along the rotating rod, as presented in Fig. 1(c). P_α generates vertical force P_v (i.e. P_v generates friction force with the friction surface) and horizontal force P_h (i.e. negative stiffness force). The lateral restoring force F of the friction plate of the key component is formulated as Eq. (1) and the force-displacement relationship is presented in Fig. 1(d).

$$F = \mathrm{sgn}(\dot{x})\mu P_v - P_h = \mathrm{sgn}(\dot{x})\mu P_\alpha \cos\alpha - P_\alpha \sin\alpha \tag{1}$$

where $P_\alpha = P/\cos\alpha$; α is the angle between the rotating rod and the initial state line, $\alpha = \arcsin\dfrac{x}{S}$, S is the length of the rotating rod; μ is the friction coefficient between the friction plate and the friction surface; and $\dot{x}$ is the velocity of the NSFDD.

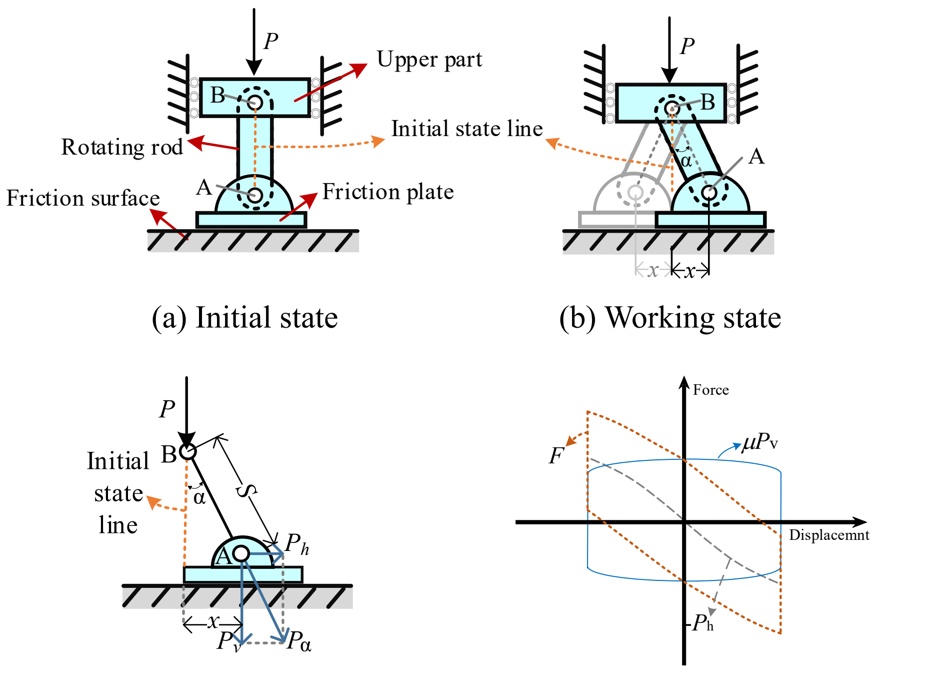

(a) Initial state (b) Working state

(c) Force diagram of working state (d) Force-displacement relationship

Fig. 1 Schematic drawing of key components of the NSFDD

2.2 Amplification mechanism

According to Eq. (1), negative stiffness and friction damping are proportional to the vertical compressive force P. To meet the response control demand of a building structure, the magnitude of the force P should be large enough to yield sufficient negative stiffness and friction damping. Using a mechanism to amplify the force P is an effective solution to improve the mechanical performance of the NSFDD. In this study, the two-consecutive lever is adopted as the amplification mechanism.

The two-consecutive lever is a mechanical device in which two levers are superimposed to achieve twofold amplification of vertical force, as depicted in Fig. 2(a). Due to the overlapping lever arms of the first-stage lever and the second-stage lever, the horizontal space is considerably reduced (compared with the classical lever). For an example as illustrated in Fig. 2, amplifying the vertical force by 15 times, the horizontal space of the two-consecutive lever is approximately 7.4-unit lengths, while the classical lever is approximately 13-unit lengths. The reduction of the occupied horizontal space is essential for application of this device in building structures.

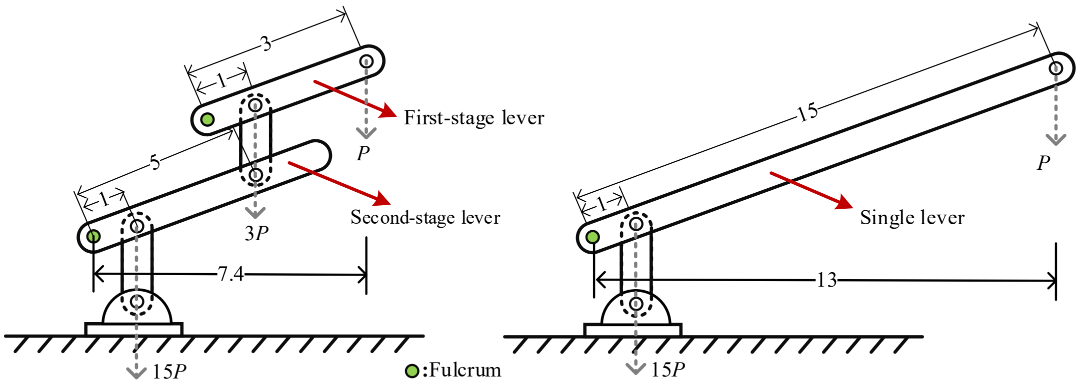

(a) Schematic of the two-consecutive lever　　(b) Schematic of the classical lever

Fig. 2 Comparison of the lever mechanisms

2.3 The mechanism of the NSFDD with an amplification mechanism

Combining the key component in Section 2.1 with the two-consecutive lever in Section 2.2, a NSFDD with an amplification mechanism is designed as shown in Fig. 3(a). The NSFDD is composed of a top plate, base plate, restraint frame, friction plate, rotating rod (I and II), and two-consecutive lever (first-stage lever and second-stage lever). Points C and K are the fulcrum of the two levers; points E and B are the resistance points of the two levers; points D and M are the power points of the two levers. The lever rotates freely with the fulcrum (points C and K). At the initial state, the force P acts vertically on point M. The vertical force amplified by the first-stage lever is P_1. The force P_1 acts vertically on point D through the rotating rod I (because the rotation angle of rotating rod I is extremely small during the working state, it is assumed that rotating rod I vertically compresses point D). The vertical force that is further amplified by the second-stage lever is denoted as P_2. The force P_2 acts vertically on point A through the rotating rod II to compress the friction plate.

The mechanical model for the restoring force F_n of the friction plate of the NSFDD with the two-consecutive lever is given by:

$$F_n = n\left(\mathrm{sgn}(\dot{x})\mu P_v - P_h\right) \tag{2}$$

where $n=L_1L_3/(L_2L_4)$ is the amplification coefficient of the two-consecutive lever, L_1, L_2 are the lengths of the long and short arms of the first-stage lever, respectively; and L_3, L_4 are the lengths of the long and short arms of the second-stage lever, respectively.

Under one cycle of loading, the hysteresis curve is generated by the friction plate of NSFDD, the process for which is as follows:

(1) As depicted in Fig. 3(b), when performing positive loading, the friction plate moves from the initial state to the positive displacement and drives the rotating rod II to rotate to the right. The force along the rotating rod II generates horizontal negative stiffness force and vertical force associated with friction force at the interface. By summarizing the horizontal negative stiffness force and friction force, the force-displacement relationship in the positive loading direction is shown in Fig. 3(c).

(2) As depicted in Fig. 3(d), when performing positive unloading, the friction plate moves from the maximum positive displacement to the initial state and drives the rotating rod II to rotate to the left, generating the force-displacement relationship shown by the blue arrow in Fig. 3(e).

(3) As depicted in Fig. 3(f), when performing negative loading, the friction plate moves from the initial state to the negative displacement and drives the rotating rod II to rotate to the left,

generating the force-displacement relationship shown by the red arrow in Fig. 3(g).

(4) As depicted in Fig. 3(h), when performing negative unloading, the friction plate moves from the maximum negative displacement to the initial state and drives the rotating rod II to rotate to the right, generating the force-displacement relationship shown by the blue arrow in Fig. 3(i).

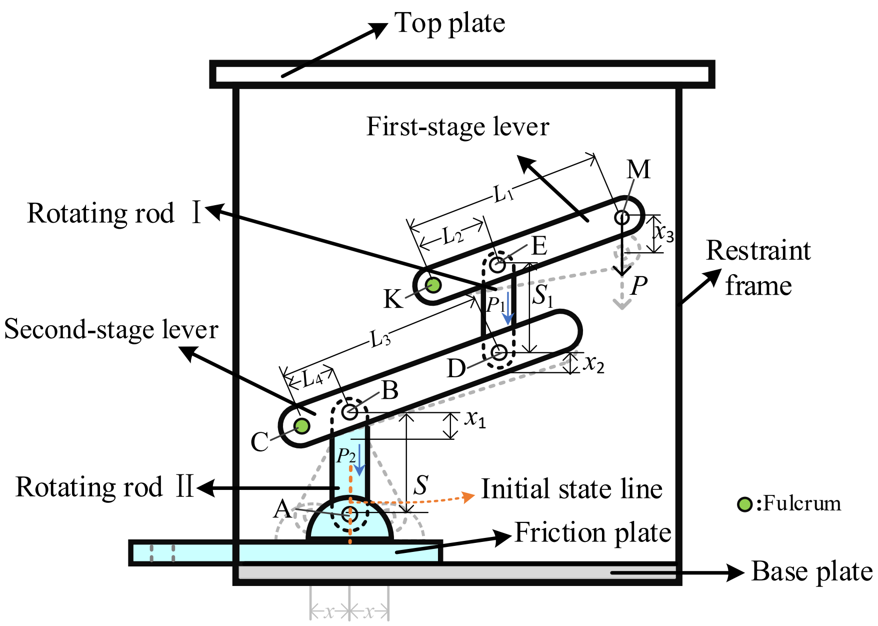

(a) Schematics of the NSFDD

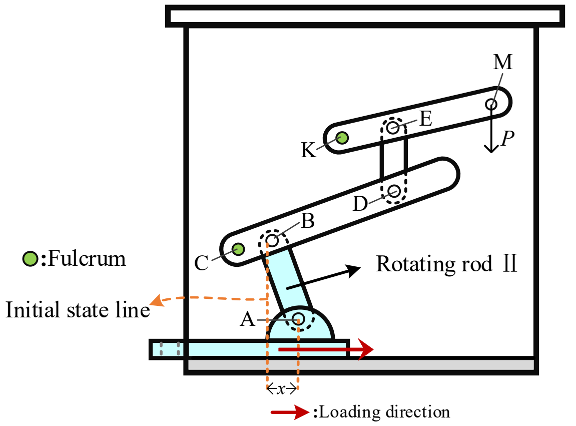

(b) Positive loading state

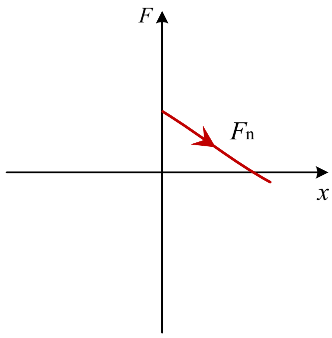

(c) Force-displacement relationship for positive loading

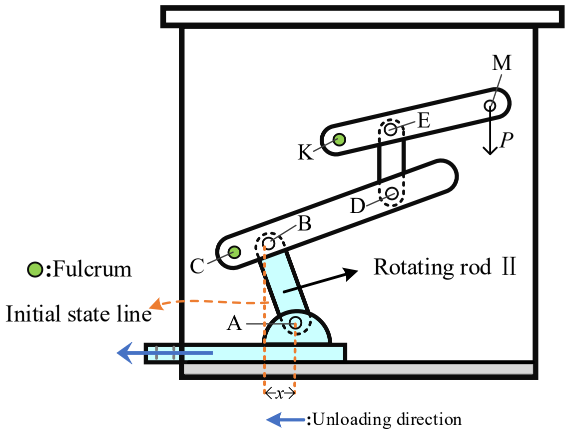

(d) Positive unloading state

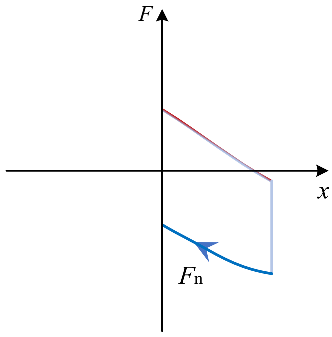

(e) Force-displacement relationship for positive unloading

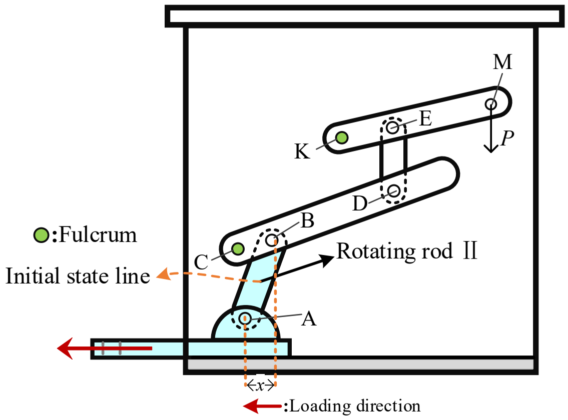

(f) Negative loading state

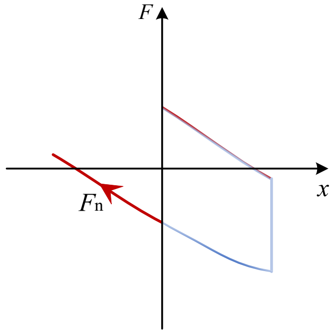

(g) Force-displacement relationship for negative loading

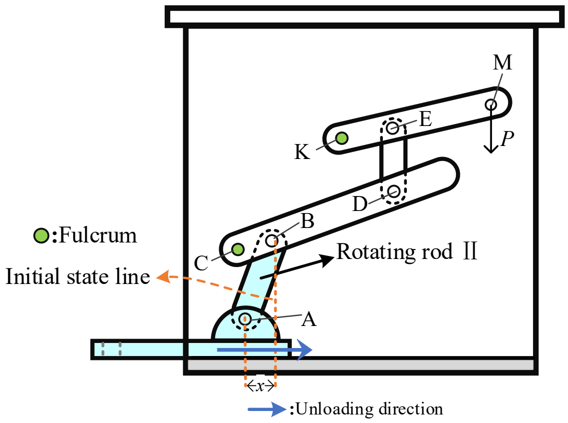

(h) Negative unloading state

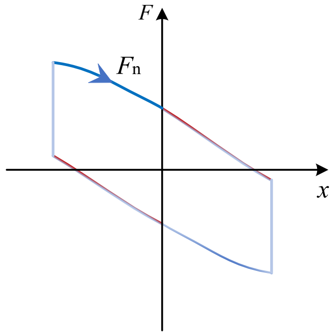

(i) Force-displacement relationship for negative unloading

161 Fig. 3 Schematics and working principle of the NSFDD with an amplification mechanism

As shown in Fig. 3(a), point B of the rotating rod II moves downward when the NSFDD has horizontal displacement (i.e., gray dashed line). The vertical geometric displacement of point B is calculated as x_1, $x_1 = S - \sqrt{S^2 - x^2}$. Because the lever principle amplifies the force and the vertical displacement, the vertical displacement x_3 at the point M is:

$$x_3 = nx_1 \tag{3}$$

As the vertical force P is commonly provided by the compressed spring, the vertical displacement x_3 at the loading point M may cause a rapid decrease in the compressed spring force.

Fig. 4 depicts the installation of a NSFDD in a floor of a building structure. The top plate and friction plate of the NSFDD are fixed to the upper and lower floor, respectively. In a positive displacement, which is defined as the lower floor moving to the right relative to the upper floor, the friction plate is forced to move to the right, causing the rotating rod II to rotate to the right (as illustrated in Fig. 4 (b)). In this condition, the pre-compressed spring moves downward, which results in a release of the pre-compressed deformation of the spring (i.e. x_3, as indicated in the red line in Fig. 4). Similarly, the deformation of the elements of NSFDD is also demonstrated in Fig. 4(d) at a negative displacement (i.e., the lower floor moves to the left relative to the upper floor). Therefore, the selection of suitable springs that remain stable compressive force within a range of deformation is vital for ensuring robust mechanical properties of the NSFDD.

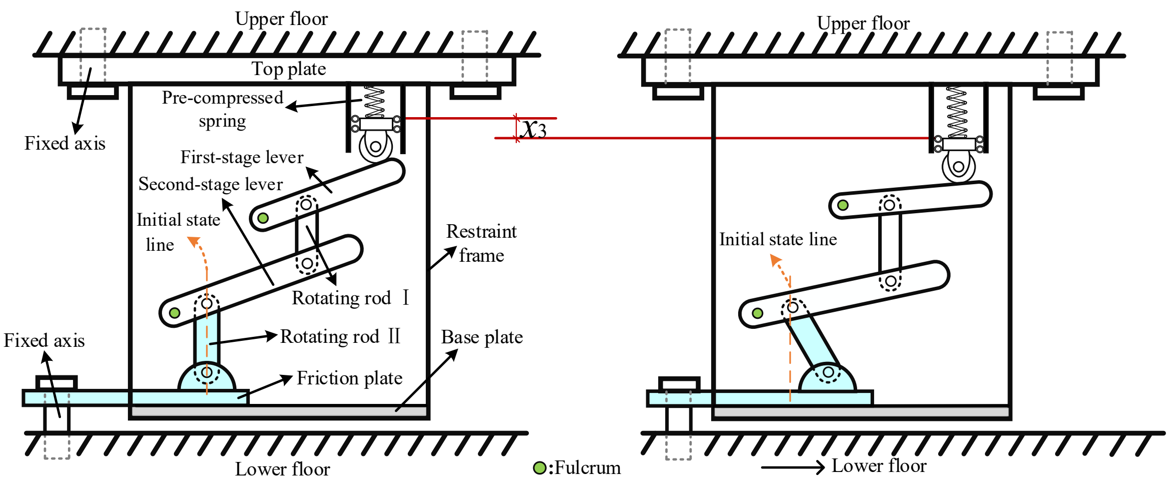

(a) zero displacement I (b) Positive displacement

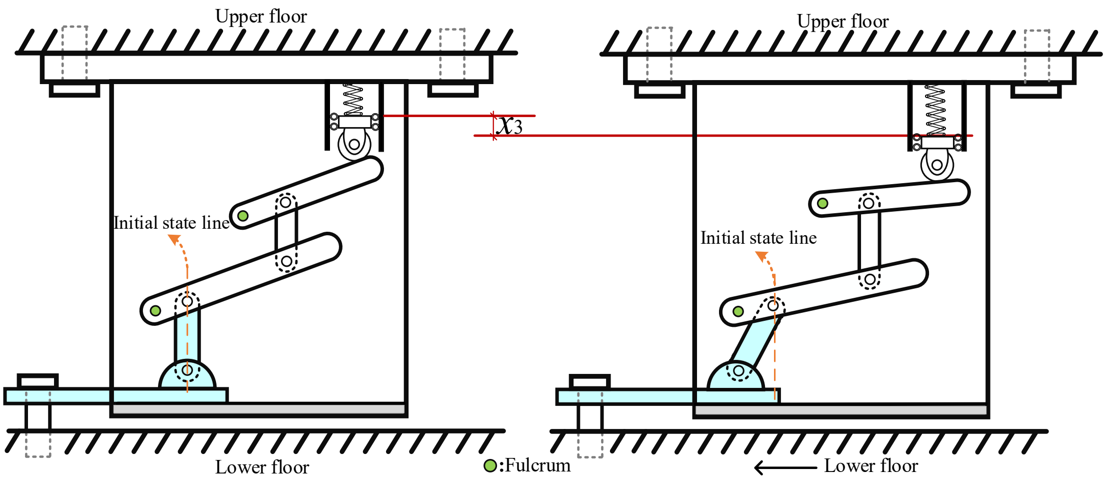

(c) zero displacement II (d) Negative displacement

Fig. 4 Deformation mechanism of the NSFDD

3. Mechanical model and parametric analysis of NSFDD

3.1 Compressed springs

In this section, the mechanical properties of a mold coil spring and gas spring are compared in light of the effectiveness of use in the NSFDD. A mold coil spring is made of chromium alloy steel with a rectangular section (see Fig. 5 (a)). Most existing negative stiffness devices use the mold coil springs, as they offer greater stiffness and durability than normal springs.

The compressed force of a mold coil spring, N_m, is calculated as:

$$N_m = k_m \Delta x \tag{4}$$

where k_m is the mold coil spring stiffness and Δx is the pre-compressed deformation.

The gas spring is a new type of spring element in which high-pressure gas is sealed within a cylinder by a piston rod. When the piston rod is forced to compress the high-pressure gas, the gas spring gains elastic stiffness from the reaction force-deformation of the high-pressure gas. A unique characteristic of a gas spring is a large initial compressive force, which is transferred from the contact force of the cylinder once the piston has an extremely small displacement (see Fig. 5 (b)). The pre-compressed gas spring force [51], N_g, can be calculated as:

$$N_g = k_g \Delta x + b \tag{5}$$

where k_g is the gas spring stiffness; and b denotes the initial compressive force.

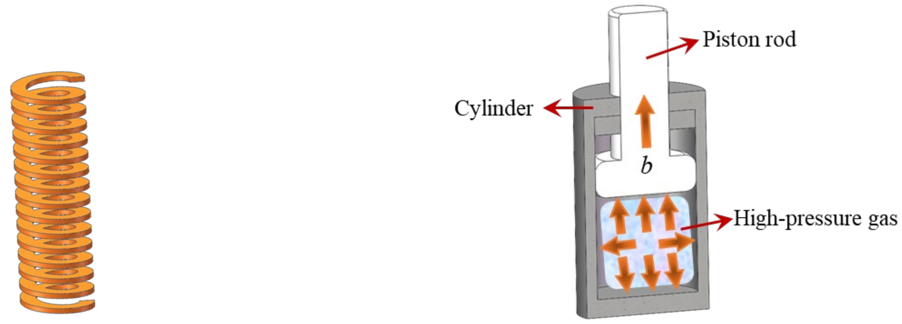

(a) Mold coil spring (b) Gas spring

Fig. 5 Diagram of two types of springs

Fig. 6 depicts the force-displacement relation of a mold coil spring and a gas spring that have identical stiffness. As the initial compressive force occupies a large portion of the total force of the gas spring, the force variation results from the displacement change occupies a smaller percentage of the total compressed force, compared to the mold coil spring. This property makes the gas spring more suited for use in NSFDD, because it can remain large compressive force within a variation of deformations. A quantitative analysis of this property will be presented in the following subsection. Except for this, the gas springs have another two advantages. First, with increased pressure of a gas, the force capacity of a gas spring can reach several times that of the mold coil spring if both springs have similar geometric dimensions. Second, a gas spring can remain stable mechanical properties even after a million cycles of loading, which enable it a long service life against fatigue.

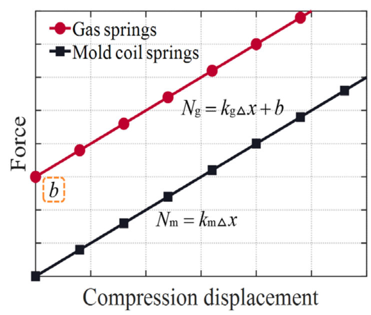

Fig. 6 Comparison of spring force between gas springs and mold coil springs

3.2 Mechanical model

3.2.1 Mold coil spring

If using the mold coil spring provides the pre-compressed force P, the mechanical model of the NSFDD can be obtained by substituting Eq. (4) into Eq. (2), given by:

$$F_{\mathrm{m}} = n\,\mathrm{sgn}(\dot{x})\mu P_{\mathrm{vm}} - nP_{\mathrm{hm}} = n\left(k_{\mathrm{m}}\left[\Delta x - n\left(S - \sqrt{S^2 - x^2}\right)\right]\right) \times \left(\mathrm{sgn}(\dot{x})\mu - \frac{x}{\sqrt{S^2 - x^2}}\right) \tag{6}$$

Fig. 7 plots a hysteretic response of an example NSFDD which is obtained by Eq. (6) and using assumed typical values for the parameters (i.e., n = 15, μ = 0.3, k_{g} = 92 kN/m, S = 60 mm, and Δx = 100 mm). As indicated in Fig. 7(a), the horizontal force P_{hm} generated by the mold coil springs provides negative stiffness at small displacements in the O_{h1}-A_{h1} and O_{h1}-B_{h1} phases. At large displacements, because the rotation of the levers reduces the pre-compressed deformation of the mold coil spring and the corresponding compressed force P, negative stiffness at the larger displacements in A_{h1} and B_{h1} is not significant. As depicted in Fig. 7(b), the vertical force P_{vm}, generated by the mold coil spring, compresses the friction plate, causing friction damping when the friction plate moves. Similarly, at large displacements (e.g., points A_{v1}, B_{v1}, C_{v1}, and D_{v1} in Fig. 7(b)), the pre-compressed deformation and corresponding force of the mold coil spring are significantly reduced, leading to an obviously reduced friction damping force. With a combination of the negative stiffness part and friction damping part, the total hysteretic response of the NSFDD is shown in Fig. 7(c). At larger displacements (e.g., points A_1, B_1, C_1, and D_1), the performance becomes unsatisfactory, because the pre-compressed spring force of the mold coil spring is significantly decreased.

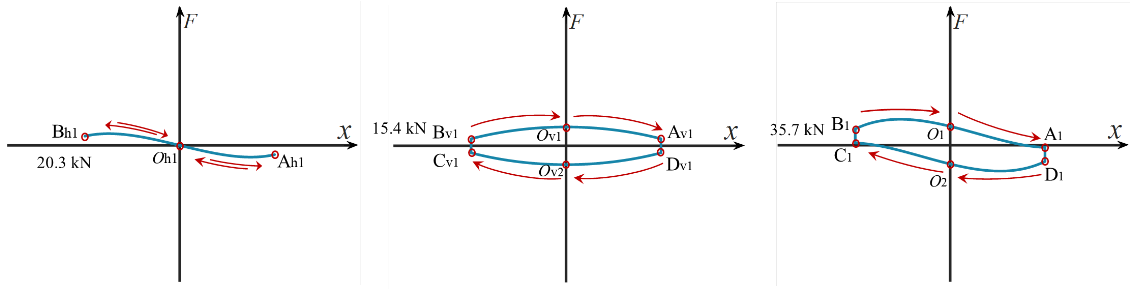

(a) Negative stiffness part (generated by P_{hm})

(b) Friction damping part (generated by P_{vm})

(c) Mechanical model of NSFDD

Fig. 7 Force-displacement relationship of the NSFDD using mold coil springs

3.2.2 Gas spring

If using the gas spring to provide the pre-compressed force P, the mechanical model of the NSFDD can be obtained by substituting Eq. (5) into Eq. (2), given by:

$$F_{\mathrm{g}} = n\,\mathrm{sgn}(\dot{x})\mu P_{\mathrm{v}} - nP_{\mathrm{h}} = n\left[k_{\mathrm{g}}\left[\Delta x - n\left(S - \sqrt{S^2 - x^2}\right)\right] + b\right] \times \left(\mathrm{sgn}(\dot{x})\mu - \frac{x}{\sqrt{S^2 - x^2}}\right) \tag{7}$$

Fig. 8 plots a hysteretic response of an example NSFDD calculated by Eq. (7). In this calculation, the value of b is taken as 16 kN, while the values for parameters in Eq. (7) are assumed to be identical to those values of mold coil spring used in Fig. 7. As indicated in Fig. 8(a), the horizontal force P_{h} generated by the gas springs provides stable negative stiffness in the O_{h2}-A_{h2} and O_{h2}-B_{h2} phases. At large displacements (e.g., A_{h2} and B_{h2}), negative stiffness remains substantial, because a high-level compressed force is maintained in the gas spring owing to the initial compressive force.

Fig. 8(b) depicts the friction force generated by P_{v}, i.e., the first term in Eq. (7). The hysteretic curve is similar as the Coulomb damping, excepting for a slight variation of the friction force at different displacement magnitudes. Such variation in the friction is induced by the changes of the pre-compressed force of the gas spring. At zero displacement (e.g., points O_{v3}, O_{v4} in Fig. 8(b)), the pre-compressed force of the gas spring has the maximum values. At large displacement (e.g., points A_{v2}, B_{v2}, C_{v2}, and D_{v2} in Fig. 8(b)), the geometric vertical displacement of the lever arm results in a release of the pre-compressed deformation and corresponding force of the gas spring.

With a combination of the negative stiffness part and friction damping part, the total hysteretic response of the NSFDD is shown in Fig. 8(c). Compared with Fig. 7(c), the pre-compressed gas springs can ensure the NSFDD has robust mechanical properties at large displacements.

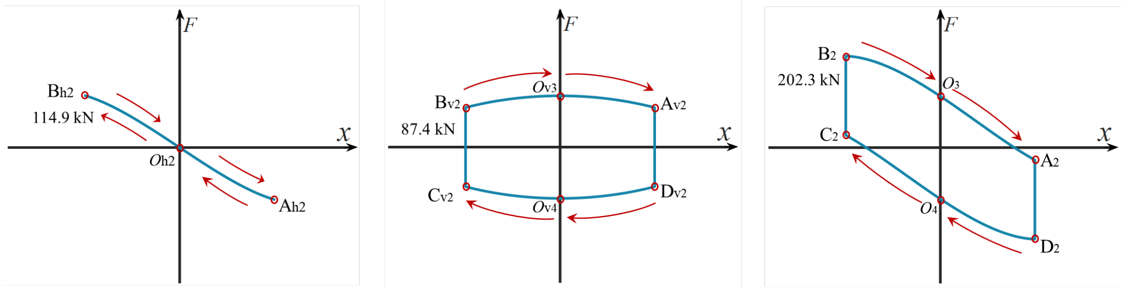

(a) Negative stiffness part (generated by P_h)

(b) Friction damping part (generated by P_v)

(c) Mechanical model of NSFDD

Fig. 8 Force-displacement relationship of the NSFDD with pre-compressed gas springs

3.2.3 Parametric analysis of NSFDD

This section discusses the effect of various parameters on the two important design indices of the NSFDD, i.e., the negative stiffness and energy dissipation. The tangent stiffness k of the NSFDD is obtained by differentiation of Eq. (7) with respect to displacement x, given by:

$$
\begin{aligned}
k = & -n\left(\frac{x^2}{\left(S^2-x^2\right)^{3/2}}+\frac{1}{\sqrt{S^2-x^2}}\right)\times\left(k_g\left(\Delta x-n\left(S-\sqrt{S^2-x^2}\right)\right)+b\right) \\
& -\frac{n^2 k_g x\left(\operatorname{sgn}(\dot{x})u-\dfrac{x}{\sqrt{S^2-x^2}}\right)}{\sqrt{S^2-x^2}}
\end{aligned}
\tag{8}
$$

From Section 3.2.2 we know that the values of amplification coefficient n and the parameters (b, k_g, and Δx) of gas springs affect the horizontal force component P_h, eventually influencing the negative stiffness value. From Eq.(7), it can be seen that the increase of the amplified vertical force P_v and friction coefficient results in a linear increase of energy dissipation. The length of rotation rod II influences its rotation angle in a given displacement, thus directly influencing the negative stiffness. The increase of the length S of rotation rob II results in a decrease of the rotation angle in a given displacement, and thus a decrease of negative stiffness. Therefore, the negative stiffness is inversely proportional to the length S.

Fig. 9 depicts the influence of the length of rotating rod II (ranging from 60 to 100 mm) and the amplified vertical force P_v (ranging from 140 to 150 kN) on the stiffness (from Eq (8)) of the NSFDD at displacement magnitude 20 mm displacement. The figure further confirms the aforementioned influence of both factors. In practical design, the design value of negative stiffness can be achieved by adjusting those two factors. As indicated in Fig. 9, the length of the rotating rod II inversely affect the negative stiffness of the NSFDD, while the amplified vertical force is proportional to the negative stiffness values of the NSFDD.

Energy dissipation is another important index for the NSFDD. The energy dissipated in a loading cycle can be calculated by integrating the NSFDD force along with the displacement. In this calculation, the displacement magnitude is ± 20 mm, and the length of rotating rob II S = 80 mm. The amplified vertical force (ranging from 140 to 150 kN) and friction coefficient (ranging from 0.1 to 0.3) are taken as variables. As indicated in Fig. 10, an increase of both amplified vertical force and friction coefficient leads to a linear increase of energy dissipation. The adjustment of both factors can be considered, to achieve the designed target energy dissipation capacity.

To conclude, the amplified vertical force P_v value linearly influences both the negative stiffness value and energy dissipation capacity of NSFDD, while the length of the rotating rod II and friction coefficient influence the negative stiffness value and energy dissipation capacity of the NSFDD, respectively. A strategic adjustment of three parameters should be performed to realize the design target values of the negative stiffness and energy dissipation of the NSFDD.

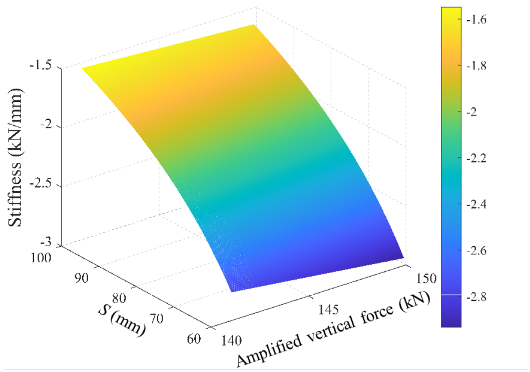

Fig. 9 Influence on negative stiffness

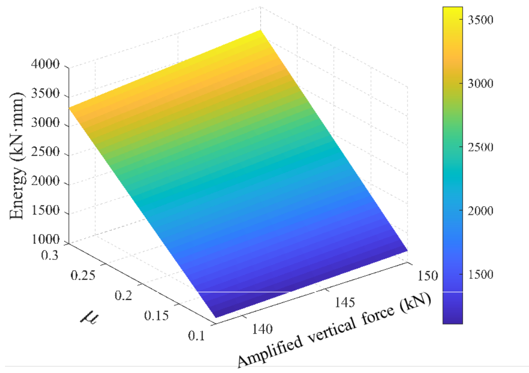

Fig. 10 Influence on energy dissipation

4 Experiments of the NSFDD

4.1 Experimental specimen

The experimental specimen is composed of the pre-compressed spring system, top plate, base plate, restraint frame, friction plate, rotating rod (I and II), and two-consecutive lever (first-stage lever and second-stage lever), as depicted in Fig. 11. The pre-compressed spring system is fixed on the top plate. The pre-compressed gas spring force is applied to the first-stage lever through the track wheel, amplified by a two-consecutive lever, and eventually transmitted to the friction plate through the rotating rod. The geometric dimensions of the experimental specimen as shown in Fig. 11(c).

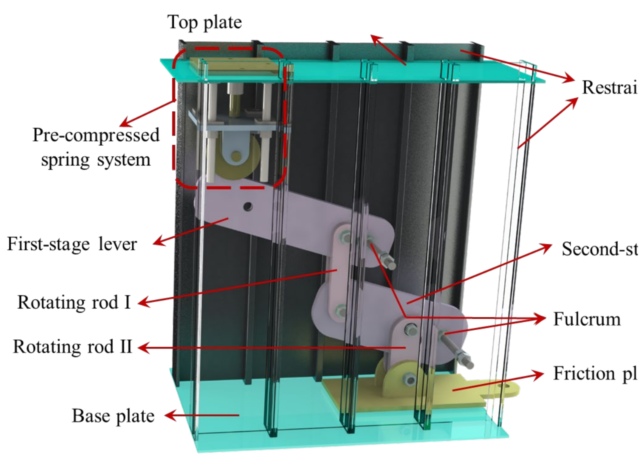

(a) Detailed 3D model (internal display)

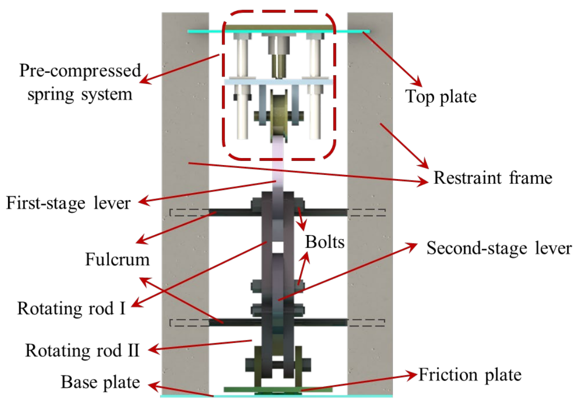

(b) Detailed 3D model (side display)

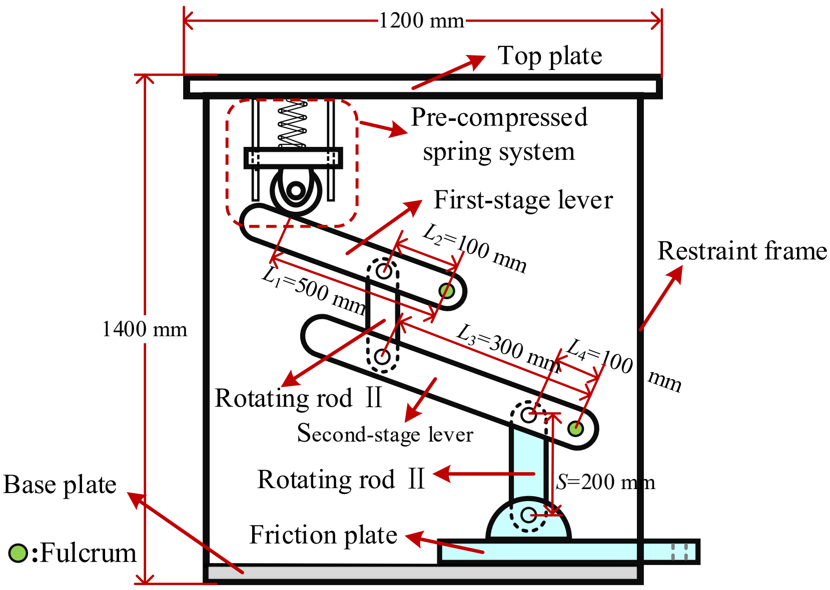

(c) Geometric dimensions

Fig. 11 Experimental specimen of the NSFDD

As shown in Fig. 12(a), when the lever is compressed by F_a, the rotating rod exerts an upward force F_b on the middle of the lever and the fulcrum exerts a downward force F_c on the lever. Therefore, the lever exerts the upward force F_d on the middle of the fulcrum and the restraint frame exerts the downward reaction force F_e on the ends of the fulcrum, as shown in Fig. 12(b). The concentrated forces at two fulcrums are eventually transferred to the restraint frame, and they are self-balanced. Therefore, the reaction force at the fulcrums does not affect the performance of the device and adjacent structural components.

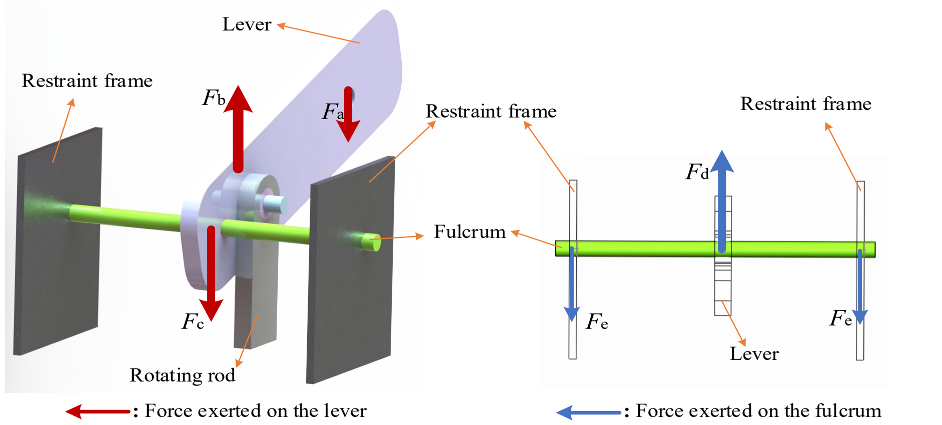

(a) Force exerted on the lever (b) Force exerted on the fulcrum

Fig. 12 Analysis of forces on the fulcrum

As shown in Fig. 13, the spring system is specifically designed to ensure the stable application of a vertical force to the lever arm. Two ends of the gas spring are connected to the top plate and a transmission plate by bolts. Four corners of the transmission plate are provided with linear bearings which passed through smooth rods fixed on the top plate, ensuring that two plates (top plate and transmission plate) are always parallel to each other during the movement. A track wheel is adopted to connect the transmission plate and the lever arm beneath it. The lever arm is placed in the groove of the track wheel, and thus the level arm maintained stable contact by small rotation of the track wheel when it moves up and down. The number of gas springs and the initial distance between the top plate and transmission plate can be adjusted to meet the design requirements of the NSFDD mechanical properties.

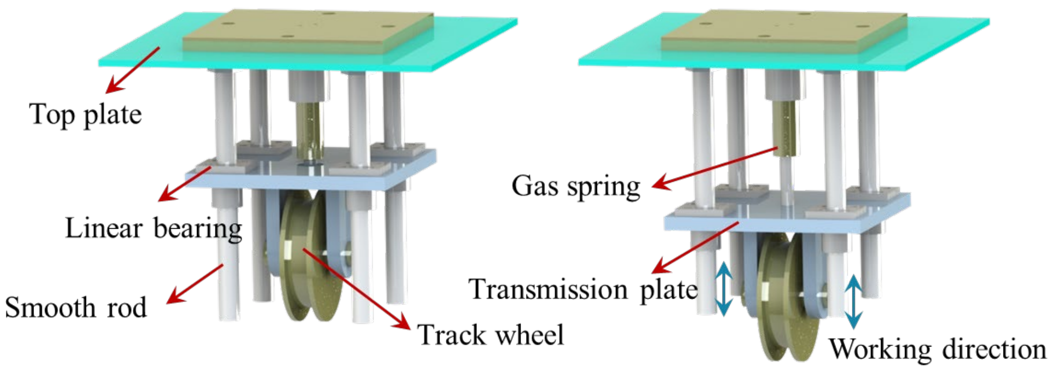

(a) Initial state (b) Working state

Fig. 13 Detailed 3D model of the pre-compressed spring system

4.2 Experimental results

Fig. 14 shows the photographs of the experimental specimen of the NSFDD. The restraint frame made of I-shaped steel beam is connected to the top and base steel plates by welding. The fulcrum of the lever arms are connected to the restraint frame. The friction plate consisted of a steel plate and four brake pads (its length, width, and thickness are all 100, 80, and 15 mm, respectively) fixed at its bottom surface. The brake pads are made of a phenolic resin composite mixed with copper flakes. The initial compressive force and stiffness of the gas spring are 16 kN and 120 kN/m, respectively. By applying the pre-compressed deformation of 100 mm, the gas spring have a compressive force equal to 28 kN. The pre-compressed gas spring force is further amplified 15 times by the two-consecutive lever. The kinetic friction coefficient between the brake pad and the surface of the steel base plate was determined as 0.29 by friction coefficient measurement tests. The test was loaded at a loading velocity of 2 mm/s. In the friction coefficient measurement tests, the size and shape of the brake pad were identical to those in the experimental tests of the NSFDD. The base plate of the NSFDD specimen is fixed with the foundation beam of the reaction frame through three steel boxes by welds and bolts. The specimen is loaded by a horizontal actuator that is connected to the friction plate. The cyclic loading is displacement controlled. Two loading cases are considered in this test. The displacement magnitude is ± 20 mm for loading case 1 and ± 30 mm for loading case 2. For both loading cases, the loading is repeated by 10 cycles. The horizontal force was measured by the load cell in the actuator, and the displacement was measured by the string potentiometer.

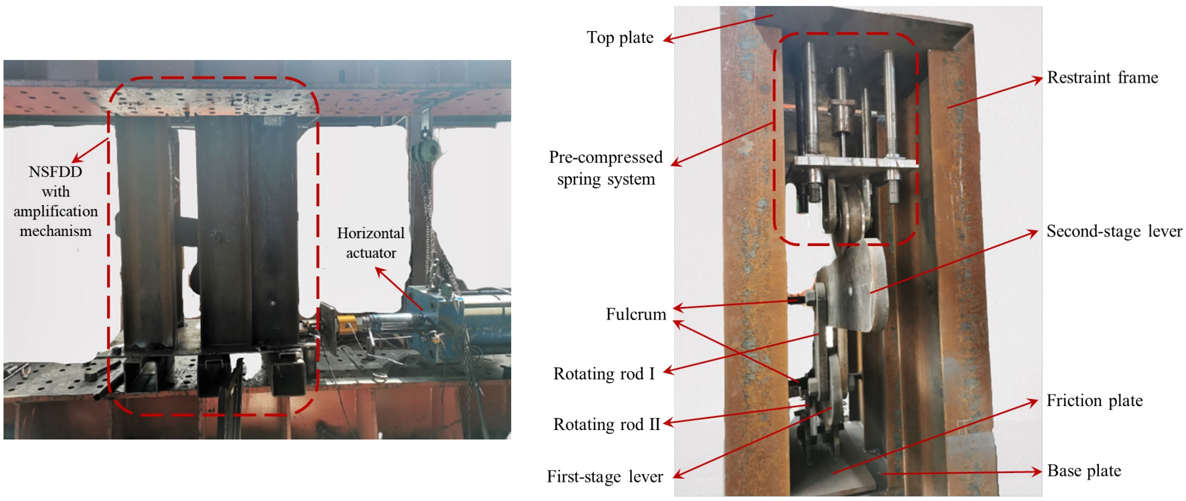

(a) Front view of the NSFDD (b) Display of the internal components of the NSFDD

Fig. 14 Photographs of experimental specimen of the NSFDD

Fig. 15 presents the hysteretic responses of the lateral force versus displacement relationship of the NSFDD specimen for two loading cases. The hysteretic curves clearly indicate a characteristic of combined negative stiffness and friction damping. During ten cycles of loading, the hysteretic response remained very stable without performance degradation. Due to the amplification mechanism of the two-consecutive lever, the small-scaled NSFDD specimen could reach the maximum lateral force of 150.9 and 174.5 kN for loading cases 1 and 2, respectively. The NSFDD specimen achieved a high amount of energy dissipation per unit weight, which is approximately 12.4 and 17.9 j/kg for loading cases 1 and 2. The efficiency of energy dissipation is higher than the conventional negative stiffness device (e.g., the device in Reference [4] have the energy dissipation per unit weight of about 0.52 j/kg). Note that the negative stiffness metamaterials can achieve even higher energy dissipation efficiency (e.g., the negative stiffness honeycomb materials [52] have the energy dissipation per unit weight of 50 - 160 J/kg).

The hysteretic curves calculated using the theoretical model (i.e., Eq. (7)) are also plotted in the Figure. The theoretical results correlated well with the experimental data. The energy dissipation in one cycle calculated from the theoretical model was consistent with the experimental results, with an average discrepancy of 2.2%. A slight difference of lateral forces was observed in the large displacement of positive loading. In addition, at the transmission point from loading to unloading, slight displacement occurred in the experimental curves because small gaps existed between the pins and the hole of the levers and rods. Such small gaps are not considered in the theoretic model.

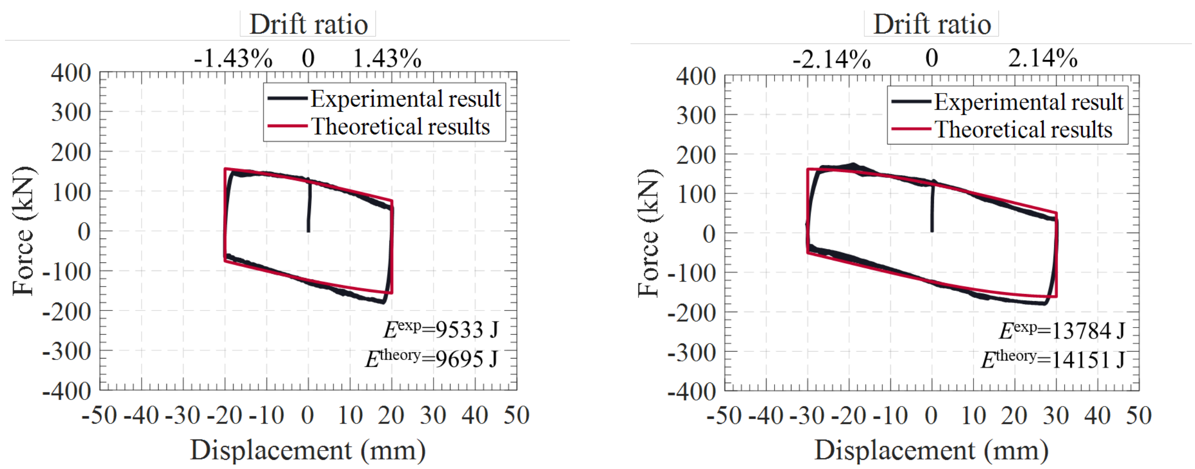

(a) Loading case 1 (b) Loading case 2

Fig. 15 Comparison of experimental and theoretical results of the NSFDD

(Note: E denotes the energy dissipated in one cycle of loading, subscribes exp and theory denote the results of the experimental test and theoretic model analysis, respectively.)

5 Finite element analysis of the NSFDD

A finite element (FE) model is developed using ABAQUS software to simulate the behavior of the NSFDD. The objective of this FE analysis is to validate the assumptions used in the development of the mechanical model (e.g., ignoring the rotation angle of rotation rob I and the weight of the lever), and to simulate the behavior of large-capacity NSFDDs.

5.1 Finite element model

The FE model is used to represent the experimental specimen in Section 4. Except for the pre-compressed gas spring, all components of the NSFDD is modeled by the solid element C3D8R, as shown in Fig. 16. The steel material is simulated by a linear model because the steel does not yield in the experimental tests. The elastic modulus and the Poisson's ratio of the steel are taken as 2.06×10^5 MPa and 0.3, respectively. The nodes of the hole surface at C and K (see Fig. 16) are constrained with the reference points that represented the fulcrum of the lever arms. Surface-to-surface discretization is achieved by the friction plate and the base plate ("hard" contact and the tangential behavior are adopted). The four brake pads with actual geometric dimensions are modeled in the friction plate bottom of the finite element model and the friction coefficient is set to 0.29. All DOFs of nodes of the base plate are fixed.

The pre-compressed gas spring is modeled using the "wire feature" in ABAQUS software. The parameters of the "wire feature" are assigned according to the mechanical properties of the gas spring, i.e., stiffness of 120 kN/m, initial compressive force of 16 kN, and the pre-compressed deformation of 100 mm. The nodes of the hole surface at M (see Fig. 16) are constrained with a reference point, and this reference point is connected to the simulated gas spring, such that the pre-compressed force is applied to the lever arm. Note that the simulation also considers the gravity loads of NSDFF self-weight. The horizontal cyclic displacement load is applied to the friction plate, with the displacement magnitude of ±20 mm and ±30 mm.

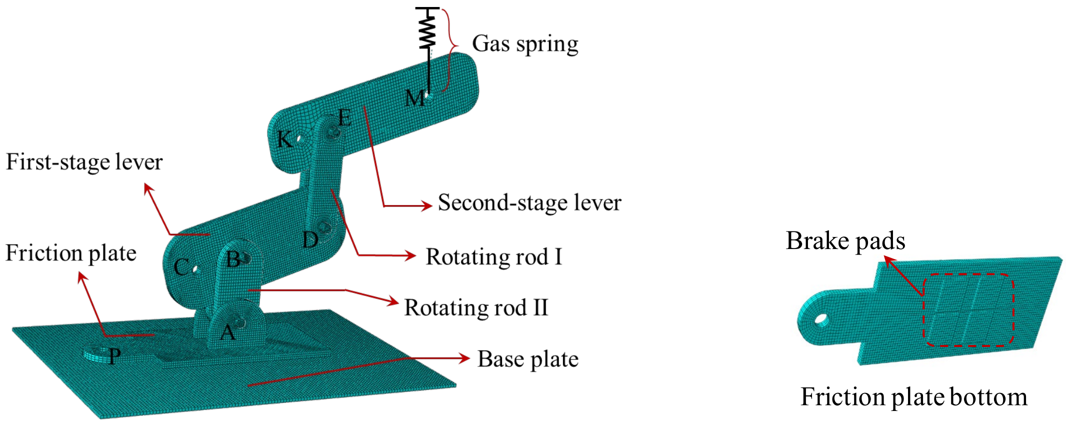

Fig. 16 Finite element model of the NSFDD with amplification mechanism

5.2 FE analysis results

The hysteretic curves of the NSFDD at loading displacement magnitude of ±20 mm and ±30 mm is obtained by FE simulation, as presented in Fig. 17. The experimental results and theoretical results using Eq. (7) are also plotted in the figures. It is indicated that the hysteretic curves of FE simulation are nearly identical to the theoretical results, and both correlate well with the experimental data. Note that the theoretical model neglects the possible influence of the NSFDD self-weight and the rotation angle of rotating rob I, while both of them are considered in the FE simulation. The comparison of the results indicates that such neglection in the simplified theoretic model is reasonable, as it does not lead to errors in estimated hysteretic responses of the NSFDD.

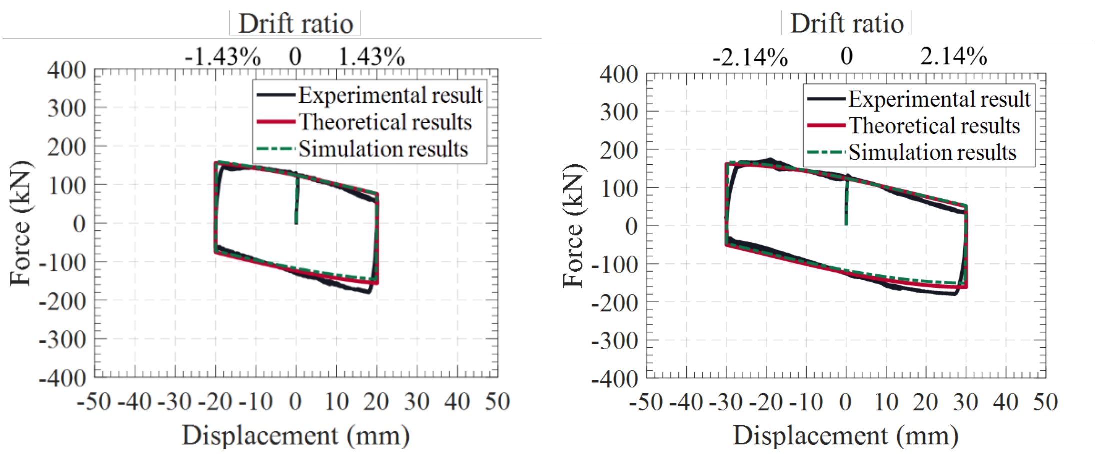

(a) Loading case 1 (b) Loading case 2

Fig. 17 Comparison of FE analytical results with experimental and theoretical results

5.3 Simulation of large-capacity NSFDD

The effect of influencing parameters is further investigated using the FE model. To realize large-capacity of devices that are commonly used in the building structures, three gas springs are included in the FE model, while the geometry and other parameters remained identical to those described in Section 5.1. Fig. 18(a) shows the hysteretic responses obtained by the FE simulation, where the maximum force reaches approximately 500 kN at 30 mm displacement.

Two key parameters are considered as the variables. One is the length of rotation rob II that primarily influences the negative stiffness value, and another is the friction coefficient that primarily affects the friction force and energy dissipation. As shown in Fig. 18(b), when the length of the rotating rod II is taken as 100, 200, and 300 mm, the tangent stiffness around zero displacement for the NSFDD model is -13.32, -6.66, and -4.44 kN/mm, respectively. The length of the rotating rod inversely affects the negative stiffness of the NSFDD. Similarly, three values for the friction coefficient μ is considered, i.e., μ = 0.145, 0.29, 0.435. As shown in 18(c), the NSFDD force increase along with an increase of the μ value. Further calculation of the area enveloped by the hysteretic curve indicates that the increase of energy dissipated in a loading cycle is linearly proportional to the increase of the μ value. The FE simulation further validates the findings in 3.2.3.

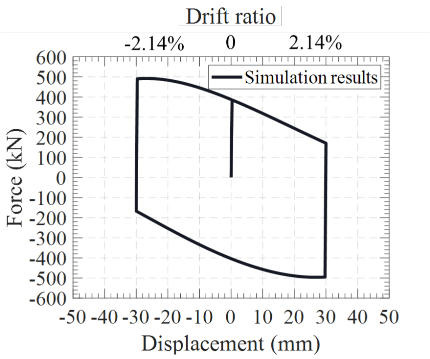

(a) Results of the large-capacity NSFDD

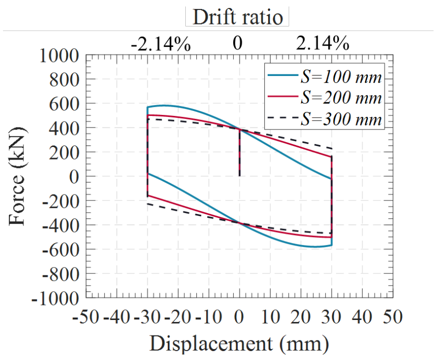

(b) Effect of rotating rod II length

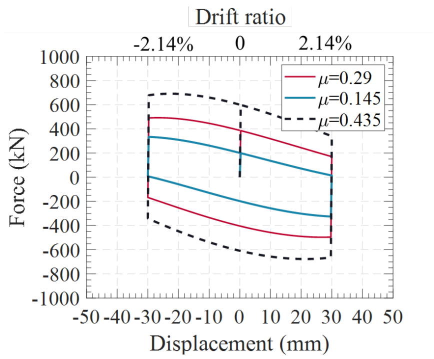

(c) Effect of friction coefficient

Fig. 18 FE analysis of hysteresis curves of large-capacity NSFDD

Conclusions

This paper proposes a novel negative stiffness friction damping device (NSFDD). This NSFDD can achieve large force capacity owing to use of the amplifying mechanism and pre-compressed gas springs. The following major conclusions are drawn from this study.

(1) A two-consecutive level and pre-compressed gas springs are used in the NSFDD. A two-consecutive level can significantly amplify the damping force. The gas spring is beneficial for maintaining stable negative stiffness and friction force in a large displacement of the NSFDD.

(2) A mechanical model of the NSFDD is proposed. The parametric analysis using the mechanical model indicates that the amplified vertical force is proportional to the negative stiffness and energy dissipation capacity of the NSFDD. The length of the rotating rod inversely affects the negative stiffness of the NSFDD, while the friction coefficient linearly influences energy dissipation capacity.

(3) The experimental tests and finite element (FE) model of the NSFDD subjected to lateral cyclic loads are conducted to examine its hysteretic behavior. The NSFDD specimen exhibits an obvious negative stiffness and stable energy dissipation, verifying the effectiveness of the proposed NSFDD. The hysteretic curves obtain from the FE model correlate well with the experimental tests data.

Acknowledgments

The authors gratefully acknowledge the National Natural Science Foundation of China (Grant No. 52178098 and No. 51421005), and the Institute for Guoqiang of Tsinghua University (Grant No. 2020GQC0003). The writers wish to express their sincere gratitude to the sponsors.

Reference

[1] Ikago K, Saito K, Inoue N. Seismic control of single-degree-of-freedom structure using tuned viscous mass damper. Earthquake Engineering and Structural Dynamics 2012; 41(3): 453-74. https://doi.org/10.1002/eqe.1138.

[2] Ji XD, Cheng YH, Hutt CM. Seismic response of a tuned viscous mass damper (TVMD) coupled wall system. Engineering Structures 2020; 225: 111252. https://doi.org/10.1016/j.engstruct.2020.111252

[3] Sarlis AA, Pasala DTR, Constantinou M C, Reinhorn AM, Nagarajaiah S, Taylor D. Negative stiffness device for seismic protection of structures–an analytical and experimental study. Proc. of 3rd ECCOMAS Thematic Conference on Computational Methods in Structural Dynamics and Earthquake Engineering, Corfu, Greece; 2011.

[4] Sarlis AA, Pasala DTR, Constantinou MC, Reinhorn AM, Nagarajaiah S, Taylor DP. Negative stiffness device for seismic protection of structures. Journal of Structural Engineering 2013; 139(7): 1124-1133. https://doi.org/10.1061/(ASCE)ST.1943-541X.0000616

[5] Molyneux WG. Supports for vibration isolation. Aeronautical Research Council, Great Britain, 1957.

[6] Giri TR, Mailen R. Controlled snapping sequence and energy absorption in multistable mechanical metamaterial cylinders. International Journal of Mechanical Sciences 2021; 204:

106541. https://doi.org/10.1016/j.ijmecsci.2021.106541

[7] Zhang Y, Wang S, Fang H, Han H, Xu Y. Design and simulation of a damper with negative stiffness for vibration mitigation from drilling equipment to a semi-submersible platform. Shock and Vibration 2020. https://doi.org/10.1155/2020/2605381

[8] Lai Z, Sun T, Nagarajaiah S. Adjustable template stiffness device and SDOF nonlinear frequency response. Nonlinear Dynamics 2019; 96(2): 1559-1573. https://doi.org/10.1007/s11071-019-04871-4

[9] Yuan S, Sun Y, Wang M, Ding J, Zhao J, Huang Y, ... & Yang XD. Tunable negative stiffness spring using Maxwell normal stress. International Journal of Mechanical Sciences 2021; 193: 106127. https://doi.org/10.1016/j.ijmecsci.2020.106127

[10] Iemura H, Pradono MH. Advances in the development of pseudo-negative-stiffness dampers for seismic response control. Journal of Structural Control and Health Monitoring 2009; 16(7-8): 784-799. https://doi.org/10.1002/stc.345

[11] Shaw AD, Gatti G, Gonçalves PJP, Tang B, Brennan MJ. Design and test of an adjustable quasi-zero stiffness device and its use to suspend masses on a multi-modal structure. Mechanical Systems and Signal Processing 2021; 152: 107354. https://doi.org/10.1016/j.ymssp.2020.107354

[12] Gatti G, Brennan MJ, Tang B. Some diverse examples of exploiting the beneficial effects of geometric stiffness nonlinearity. Mechanical Systems and Signal Processing 2019; 125: 4-20. https://doi.org/10.1016/j.ymssp.2018.08.024

[13] Chen BC, Chen LM, Du B, Liu HC, Li WG, Fang DN. Novel multifunctional negative stiffness mechanical metamaterial structure: Tailored functions of multi-stable and

compressive mono-stable. Composites Part B: Engineering 2021; 204: 108501. https://doi.org/10.1016/j.compositesb.2020.108501

[14] Tan XJ, Wang B, Zhu SW, Chen S, ... & Sun YG. Novel multidirectional negative stiffness mechanical metamaterials. Smart Materials and Structures 2019; 29(1), 015037. https://doi.org/10.1088/1361-665X/ab47d9

[15] Tan XJ, Chen S, Wang B, Zhu SW, Wu LZ, Sun YG. Design, fabrication, and characterization of multistable mechanical metamaterials for trapping energy. Extreme Mechanics Letters 2019; 28: 8-21. https://doi.org/10.1016/j.eml.2019.02.002

[16] Tan XJ, Wang B, Yao KL, Zhu SW, Chen S, ... & Sun YG. Novel multi-stable mechanical metamaterials for trapping energy through shear deformation. International Journal of Mechanical Sciences 2019; 164: 105168. https://doi.org/10.1016/j.ijmecsci.2019.105168

[17] Zhu SW, Tan XJ, Wang B, Chen S, Hu JQ, Ma L, Wu LZ. Bio-inspired multistable metamaterials with reusable large deformation and ultra-high mechanical performance. Extreme Mechanics Letters 2019; 32: 100548. https://doi.org/10.1016/j.eml.2019.100548

[18] Tan XJ, Wang B, Chen S, Zhu SW, Sun YG. A novel cylindrical negative stiffness structure for shock isolation. Composite Structures 2019; 214: 397-405. https://doi.org/10.1016/j.compstruct.2019.02.030

[19] Zhu SW, Wang B, Tan XJ, Hu JQ, Wang LC, Zhou GZ, Chen S. A novel bi-material negative stiffness metamaterial in sleeve-type via combining rigidity with softness. Composite Structures 2021; 262, 113381. https://doi.org/10.1016/j.compstruct.2020.113381

[20] Zhu SW, Wang B, Chen LM, Tan XJ, Ma L. Enhance the energy dissipation ability of sleeve-type negative stiffness structures via a phase-difference mechanism. International

Journal of Mechanical Sciences 2022; 213, 106803. https://doi.org/10.1016/j.ijmecsci.2021.106803

[21] Meng H, Huang XC, Chen YY, Theodossiades S, Chronopoulos D. Structural vibration absorption in multilayered sandwich structures using negative stiffness nonlinear oscillators. Applied Acoustics 2021; 182: 108240. https://doi.org/10.1016/j.apacoust.2021.108240

[22] Robertson WS, Kidner MRF, Cazzolato BS, Zander AC. Theoretical design parameters for a quasi-zero stiffness magnetic spring for vibration isolation. Journal of Sound and Vibration 2009; 326(1-2): 88-103. https://doi.org/10.1016/j.jsv.2009.04.015

[23] Mehreganian N, Fallah AS, Sareh P. Structural mechanics of negative stiffness honeycomb metamaterials. Journal of Applied Mechanics 2021; 88(5): 051006. https://doi.org/10.1115/1.4049954

[24] Anastasio D, Marchesiello S. Experimental characterization of friction in a negative stiffness nonlinear oscillator. Vibration 2020; 3(2): 132-148. https://doi.org/10.3390/vibration3020011

[25] Anastasio D, Fasana A, Garibaldi L, Marchesiello S. Nonlinear dynamics of a duffing-like negative stiffness oscillator: modeling and experimental characterization. Shock and Vibration 2020. https://doi.org/10.1155/2020/3593018

[26] Salvatore A, Carboni B, Lacarbonara W. Nonlinear dynamic response of an isolation system with superelastic hysteresis and negative stiffness. Nonlinear Dynamics 2022; 107(2): 1765-1790. https://doi.org/10.1007/s11071-021-06666-y

[27] Zhu R, Marchesiello S, Anastasio D, Jiang D, Fei QG. Nonlinear system identification of a double-well Duffing oscillator with position-dependent friction. Nonlinear Dynamics 2022;

1-16. https://doi.org/10.1007/s11071-022-07346-1

[28] Iemura H, Pradono MH. Application of pseudo-negative stiffness control to the benchmark cable-stayed bridge. Journal of Structural Control 2003; 10(3-4): 187-203. https://doi.org/10.1002/stc.25

[29] Asai T, Spencer Jr BF, Iemura H, Chang CM. Nature of seismic control force in acceleration feedback. Structural Control and Health Monitoring 2012; 20(5): 789-803. https://doi.org/10.1002/stc.1496

[30] Das S, Chakraborty S, Chen Y, Tesfamariam S. Robust design optimization for SMA based nonlinear energy sink with negative stiffness and friction. Soil Dynamics and Earthquake Engineering 2021; 140: 106466. https://doi.org/10.1016/j.soildyn.2020.106466

[31] Shan J, Shi Z, Gong N, Shi W. Performance improvement of base isolation systems by incorporating eddy current damping and magnetic spring under earthquakes. Structural Control and Health Monitoring 2020; 27(6): e2524. https://doi.org/10.1002/stc.2524

[32] Nepal S, Saitoh M. Improving the performance of conventional base isolation systems by an external variable negative stiffness device under near-fault and long-period ground motions. Earthquake Engineering and Engineering Vibration 2020; 19(4): 985-1003. https://doi.org/10.1007/s11803-020-0609-3

[33] Wang Y, Li H, Cheng C, Ding Hu. Dynamic performance analysis of a mixed-connected inerter-based quasi-zero stiffness vibration isolator. Structural Control and Health Monitoring 2020; 27(10): e2604. https://doi.org/10.1002/stc.2604

[34] Cimellaro G P, Domaneschi M, Warn G. Three-dimensional base isolation using vertical negative stiffness devices. Journal of Earthquake Engineering 2020; 24(12): 2004-2032.

https://doi.org/10.1080/13632469.2018.1493004
[35] Javanbakht M, Cheng S, Ghrib F. Refined damper design formula for a cable equipped with a positive or negative stiffness damper. Structural Control and Health Monitoring 2018; 25(10): e2236. https://doi.org/10.1002/stc.2236
[36] Javanbakht M, Cheng S, Ghrib F. Multimode vibration control of stay cables using optimized negative stiffness damper. Structural Control and Health Monitoring 2020; 27(4): e2503. https://doi.org/10.1002/stc.2503
[37] Javanbakht M, Cheng S, Ghrib F. Impact of support stiffness on the performance of negative stiffness dampers for vibration control of stay cables. Structural Control and Health Monitoring 2020; 27(10): e2610. https://doi.org/10.1002/stc.2610
[38] Walsh KK, Boso E, Steinberg EP, Haftman JT, Littell WN. Variable negative stiffness device for seismic protection of building structures through apparent weakening. Journal of Engineering Mechanics 2018; 144(9): 04018090. https://doi.org/10.1061/(ASCE)EM.1943-7889.0001512
[39] Shirai K, Noro S, Walsh KK. Shake table testing of a passive negative stiffness device with curved leaf springs for seismic response mitigation of structures. Structural Control and Health Monitoring 2021; 28(7): e2736. https://doi.org/10.1002/stc.2736
[40] Sarlis AA, Pasala DTR, Constantinou MC, Reinhorn AM, Nagarajaiah S, Taylor DP. Negative stiffness device for seismic protection of structures: shake table testing of a seismically isolated structure. Journal of Structural Engineering 2016; 142(5): 04016005. https://doi.org/10.1061/(ASCE)ST.1943-541X.0001455
[41] Pasala DTR, Sarlis AA, Nagarajaiah S, Reinhorn AM, Constantinou MC, Taylor D.

Adaptive negative stiffness: new structural modification approach for seismic protection. Journal of Structural Engineering 2013; 139(7): 1112-1123. https://doi.org/10.1061/(ASCE)ST.1943-541X.0000615

[42] Nagarajaiah S, Sen D. Apparent-weakening by adaptive passive stiffness shaping along the height of multistory building using negative stiffness devices and dampers for seismic protection. Engineering Structures 2020; 220: 110754. https://doi.org/10.1016/j.engstruct.2020.110754

[43] Meng Wang, Nagarajaiah S, Sun FF. Dynamic characteristics and responses of damped outrigger tall buildings using negative stiffness. Journal of Structural Engineering 2020; 146: 04020273. https://ascelibrary.org/doi/10.1061/(ASCE)ST.1943-541X.0002846

[44] Sun FF, Meng Wang, Nagarajaiah S. Multi-objective optimal design and seismic performance of negative stiffness damped outrigger structures considering damping cost. Engineering Structures 2021; 229: 111615. https://doi.org/10.1016/j.engstruct.2020.111615

[45] Sun T, Lai Z, Nagarajaiah S, Li HN. Negative stiffness device for seismic protection of smart base isolated benchmark building. Structural Control and Health Monitoring 2017; 24: e1968. https://doi.org/10.1002/stc.1968

[46] Wang M, Sun FF,Yang JQ, Nagarajaiah S. Seismic protection of SDOF systems with a negative stiffness amplifying damper. Engineering Structures 2019; 190: 128-141. https://doi.org/10.1016/j.engstruct.2019.03.110

[47] Chen L, Sun L, Nagarajaiah S. Cable with discrete negative stiffness device and viscous damper: passive realization and general characteristics. Smart Structures and Systems 2015; 15(3): 627-643. http://dx.doi.org/10.12989/sss.2015.15.3.627

[48] Kapasakalis KA, Antoniadis IA, Sapountzakis EJ. Constrained optimal design of seismic base absorbers based on an extended KDamper concept. Engineering Structures 2021; 226: 111312. https://doi.org/10.1016/j.engstruct.2020.111312

[49] Antoniadis IA, Kanarachos SA, Gryllias K, Sapountzakis IE. KDamping: a stiffness based vibration absorption concept. Journal of Vibration and Control 2018; 24(3): 588–606. https://doi.org/10.1177/1077546316646514

[50] Sapountzakis EJ, Syrimi PG, Pantazis IA, Antoniadis IA. KDamper concept in seismic isolation of bridges with flexible piers. Engineering Structures 2017; 153: 525-539. http://dx.doi.org/10.1016/j.engstruct.2017.10.044

[51] Sun TW, Peng LY, Li X, Kang Y, Deng Y. Development and analysis of negative stiffness friction damping device. KSCE Journal of Civil Engineering 2021; 25 (7): 2587-2602. https://doi.org/10.1007/s12205-021-1282-4

[52] Correa DM, Klatt T, Cortes S, Haberman M, Kovar D, Seepersad C. Negative stiffness honeycombs for recoverable shock isolation. Rapid Prototyping Journal 2015; 21 (2): 193-202. https://doi.org/10.1108/RPJ-12-2014-0182